Electrochimica Acta 579 (2026) 149943

Contents lists available at ScienceDirect

Electrochimica Acta

journal homepage: www.journals.elsevier.com/electrochimica-acta

Surface-reconstructed Ni@Ni_3N nanocolumns via plasma nitridation for electrocatalytic hydrogen evolution

Xueqing Zhao [a,b,1], Mei Wang [c,1], Caifeng Zhang [a], Sixie Zhang [d], Guanshui Ma [a,*], Aiying Wang [a,*]

[a] State Key Laboratory of Advanced Marine Materials, Zhejiang Key Laboratory of Extreme-environmental Material Surfaces and Interfaces, Ningbo Institute of Materials Technology and Engineering, Chinese Academy of Sciences, Ningbo, 315201, China
[b] College of Chemical Engineering, Zhejiang University of Technology, Hangzhou, 310014, PR China
[c] School of Materials Science and Engineering, North University of China, Taiyuan, 030051, China
[d] State Key Laboratory of Advanced Marine Materials, Zhejiang Key Laboratory of Advanced Fuel Cells and Electrolyzers Technology, Ningbo Institute of Materials Technology and Engineering, Chinese Academy of Sciences, Ningbo, 315201, China

ARTICLE INFO

Keywords:
Nickel nitride
Hydrogen evolution reaction
Plasma nitridation
Alkaline electrocatalysis

ABSTRACT

Hydrogen production through alkaline water electrolysis requires electrocatalysts with high intrinsic activity, structural robustness, and scalable fabrication capability. Herein, we report a plasma-induced surface reconstruction strategy for directly growing vertically aligned Ni@Ni_3N nanocolumn arrays on nickel foam, enabling simultaneous structural regulation and interfacial electronic modulation during alkaline HER. Distinct from conventional surface nitridation, the plasma-assisted process promotes the spontaneous self-assembly of dense nanocolumn architectures with a nitrided layer thickness of approximately 50–80 nm, while maintaining intimate electronic interaction between the nitrided surface and metallic substrate. The integrated architecture maximizes active-site exposure and facilitates charge redistribution at the Ni/Ni_3N metal-nitride interface, thereby accelerating reaction kinetics. As a result, the optimized electrode exhibits an overpotential of 64 mV at 10 mA cm^{-2} and a Tafel slope of 36 mV dec^{-1} in 1 M KOH, with negligible activity decay after 72 h of continuous operation. Density functional theory calculations reveal that the electronic interaction between metallic Ni and surface Ni_3N modifies the electronic states near the Fermi level and optimizes hydrogen adsorption thermodynamics compared with pristine Ni_3N. Furthermore, the vertically aligned nanocolumn architecture promotes rapid electron transport and efficient bubble release. This work provides insight into plasma-induced interfacial reconstruction for nitride electrocatalysts for designing high-performance self-supported nitride electrocatalysts.

1. Introduction

In the context of the transformation of the global energy system to low-carbon, hydrogen energy is a clean and efficient secondary energy carrier, and its efficient preparation technology is the key to promote the transformation of energy structure [1,2]. At present, the production methods of hydrogen include chemical reforming, biological hydrogen production and water electrolysis [3–5]. Among them, the hydrogen evolution reaction of electrolytic water is considered to be the core path of green hydrogen production. However, it is difficult to achieve high energy conversion efficiency by simply relying on the electrochemical process of water reduction and hydrogen evolution [6,7]. The noble metal platinum-based catalyst is the best hydrogen evolution reaction (HER) catalyst with low overpotential, high exchange current density and significant reaction stability, which can effectively reduce the energy barrier of hydrolysis dissociation and improve the reaction rate [8–10]. However, its high cost and scarce reserves seriously restrict its large-scale application. Therefore, the development of efficient, stable and low-cost non-precious metal catalysts has become the focus of research in recent years [11,12].

Transition metals such as Ni, Co, Cu, W and Mo with price advantages have been proved to have good catalytic activity for hydrogen production from electrolytic water [13–15]. Transition metal-based catalysts encompass various compounds such as sulfides, borides,

* Corresponding authors.
E-mail addresses: maguanshui@nimte.ac.cn (G. Ma), aywang@nimte.ac.cn (A. Wang).
[1] Xueqing Zhao and Mei Wang contributed equally to the work.

https://doi.org/10.1016/j.electacta.2026.149943
Received 8 June 2026; Received in revised form 29 August 2026; Accepted 7 September 2026
Available online 9 September 2026
0013-4686/© 2026 Elsevier Ltd. All rights are reserved, including those for text and data mining, AI training, and similar technologies.

carbides, and nitrides [16–20]. Among these, metal sulfides often suffer from poor electrical conductivity and tend to undergo volumetric expansion during operation. Metal borides pose challenges in terms of synthesis, while metal carbides generally exhibit inadequate corrosion resistance and are prone to detachment. Metal oxides, on the other hand, are limited by their low conductivity. In contrast, transition metal nitrides (TMNs) have attracted increasing attention for alkaline HER because their tunable electronic structures and metallic conductivity can regulate interfacial charge-transfer processes and adsorption behavior of reaction intermediates [21,22]. Compared with transition metal-based materials such as Co, Fe and Mo, the Gibbs free energy (ΔG) of nickel-based catalysts for HER changes less, and the overpotential of nickel-based catalysts for HER is lower at the same current density [23]. Doping other elements can regulate the electronic structure of nickel-based catalysts, thereby further improving the activity and stability of the catalyst. Another design strategy for transition metal nitride catalysts is to change the structure of the catalyst and enhance the catalytic activity by exposing more active sites, such as building nanosheets, nanowires and nanoarrays [13,24].

The design of electrocatalytic materials with unique nanostructures can effectively increase the number of surface-active sites, enhance the intrinsic activity of these sites, and improve electrical contact. To achieve better dispersion of the active catalytic materials, researchers typically employ porous conductive substrates, such as nickel foam (NF), iron foam, and carbon fiber materials, for loading the active substances [25,26]. These substrates possess excellent conductivity, high specific surface area, and mechanical stability, which effectively prevent the aggregation and deactivation of catalytic species, increase the contact area with the electrolyte, and enhance mass and charge transfer efficiency. Furthermore, materials grown in-situ on the substrate exhibit a self-supporting nature, allowing them to be directly used as electrodes for water electrolysis. This eliminates the need for binders, such as Nafion, thereby reducing additional electrical resistance and the blocking of active sites that can hinder the catalytic process. Concurrently, the strong interaction between the in-situ grown material and the substrate contributes to superior mechanical stability, preventing detachment during long-term catalytic operation and thereby further enhancing overall durability. Zhao et al. [27] prepared a three-dimensional hierarchical catalyst based on Ni, Fe, and Co metals via a straightforward hydrothermal and electrodeposition method. The resulting electrode features a triple-layer porous architecture: a microporous nickel foam substrate (pore size ~500 μm) at the bottom, vertically aligned microporous $NiCo_2O_4$ nanosheets (~500 nm pores) grown in-situ as the intermediate layer, and mesoporous NiFe hydroxide nanosheets (~5 nm pores) in-situ grown as the top layer. This hierarchical nanostructure is binder-free, which maximizes the exposure of active catalytic sites, enhances mass and charge transfer, and facilitates the efficient release of gases generated during water electrolysis, thereby preventing the isolation of active sites from the electrolyte. When employed as a cathode for the hydrogen evolution reaction, the catalyst achieves a current density of 10 $mA{\cdot}cm^{-2}$ at a moderate overpotential of 105 mV, along with remarkable stability during prolonged operation in alkaline electrolyte. In contrast to conventional hydrothermal or thermal nitridation synthetic routes, plasma nitridation enables the controllable construction of nickel-based nitride catalytic electrodes on NF substrates. This technique utilizes highly reactive nitrogen plasma species to achieve rapid nitridation at relatively low temperatures, preserving the structural integrity of pre-grown nanostructures while allowing precise control over phase composition and morphology, thereby addressing the challenges of structural damage and poor synthetic controllability inherent to traditional nitridation methods [28]. Although Ni/Ni_3N heterostructures and self-supported nickel nitride nanoarrays have been reported, most existing synthetic routes involve multi-step procedures: pre-growth of nanostructured precursors followed by thermal or plasma nitridation. These methods often suffer from limited control over nitridation depth, possible structural damage during high-temperature treatment, and the need for additional metal sources [29]. Similarly, plasma-nitrided Ni-based catalysts reported to date frequently contain binary or ternary alloy components, making it difficult to isolate the specific role of the Ni/Ni_3N interface. By simply tuning the substrate bias voltage during plasma nitridation, commercial nickel foam can be directly transformed into vertically aligned Ni@Ni_3N nanocolumns without any template or precursor, thus providing a facile and controllable route for fabricating high-performance self-supported nitride electrodes.

In this work, plasma nitridation was employed to induce surface reconstruction on nickel foam, forming vertically aligned Ni@Ni_3N nanocolumn electrodes with coupled structural and interfacial electronic features. Combined electrochemical analysis and DFT calculations reveal that the reconstructed Ni/Ni_3N interface regulates electronic states near the Fermi level and modulates hydrogen adsorption free energy, thereby facilitating alkaline HER electrocatalytic activity.

2. Experimental methods

2.1. Plasma nitriding nickel foam

Ni_3N/ NF was prepared in a self-made physical vapor ion beam deposition equipment. NF was purchased from Kunshan Guangjiayuan New Materials Co., Ltd., China. The nickel foam was cut into a 4.0 × 4.0 cm area and cleaned in turn with acetone, ethanol and deionized water before being put into the equipment. After drying with nitrogen, the nickel foam was placed in the vacuum chamber of the ion beam deposition equipment, and Ni_3N was synthesized in situ by nitrogen plasma. During the nitriding process, the temperature was set to 500 °C. The flow rates of nitrogen and argon were 95 and 5 sccm, respectively. The nitriding treatment time was 10 h. The ion beam voltage was 2500 V, and the substrate bias was −250 V, −500 V, and −750 V, so samples obtained were named NF-250, NF-500 and NF-750, respectively.

2.2. Characterization

The microstructure of Ni_3N/NF was characterized by scanning electron microscopy (SEM, FEI Quanta FEG 250, USA). The chemical composition of Ni_3N/NF samples was characterized by X-ray photoelectron spectroscopy (XPS, Axis Ultra DLD, UK). High-resolution transmission electron microscopy (HRTEM, Talos F200x, USA) analysis was performed using a field emission.

2.3. Electrochemical test

All electrochemical characterizations were performed in a conventional three-electrode system using a Gamry electrochemical workstation at a temperature of ~ 25 °C, and the electrolyte was 1 M KOH (pH = 14). The 1.0 cm × 1.0 cm Ni_3N/NF and NF samples were used as the working electrode, the graphite rod was the counter electrode, and the Hg/HgO electrode was used as the reference electrode. Linear cyclic voltammetry (LSV) was performed at a scan rate of 10 mV s^{-1}. All polarization curves were recorded without iR compensation. Electrochemical measurements were repeated on at least three independently prepared electrodes, and representative data are shown; the reported overpotentials are average values with variations within ±5 mV. Since the Ni_3N active material is formed in situ by direct nitridation of the nickel foam substrate, no additional binder or catalyst loading was used, and the current density is reported based on the geometric area of the electrode (1 cm × 1 cm). All potentials in the experiment were converted to reversible hydrogen electrode (RHE) according to Eq. (1), and the Tafel slope was converted from linear sweep voltammetry by Eq. (2) [12]:

$$E(RHE) = E(Hg/HgO) + 0.098 + 0.05916 \times pH \quad (1)$$

$$\eta = b \times \log|j| + a \quad (2)$$

where η, b, j and a represent overpotential, Tafel slope, current density and Tafel constant, respectively. The long-term stability of the catalyst was evaluated by current density-time measurements at a constant potential. The potential is determined based on the LSV curve at 10 mA cm^{-2}. The electrochemical impedance spectroscopy (EIS) test was carried out in the frequency range from 100 kHz to 0.01 Hz with an applied AC disturbance amplitude of 10 mV. The EIS data obtained from the experiment were analyzed by equivalent circuit fitting using ZView software. A series of cyclic voltammetry (CV) experiments were carried out in 0.1 M NaOH at scan rates of 10, 20, 40, 60, 80 and 100 mV s^{-1}. By plotting the linear relationship between the $\Delta j/2$ (where $\Delta j = j_{anodic} - j_{cathodic}$) between the anode current and the cathode current and the scanning rate, the slope is calculated to be C_{dl}. Then, the ECSA is determined by dividing C_{dl} by the specific capacitance (C_s) of the material, as shown in Eq. (3).

$$ECSA = C_{dl}/C_S \quad (3)$$

Among them, Cs is usually 0.04 mF cm^{-2} in alkaline solution [30].

2.4. Theoretical calculation details

All density functional theory (DFT) calculations were performed using the Vienna Ab Initio Simulation Package (VASP). The exchange-correlation functional was treated within the Perdew-Burke-Ernzerhof (PBE) generalized gradient approximation, and the electron-ion interactions were described using the projector augmented-wave (PAW) method. A plane-wave kinetic energy cutoff of 400 eV was employed. The Brillouin zone was sampled with a Monkhorst-Pack k-point mesh of 5 × 5 × 3 for the bulk Ni_3N structure and 5 × 5 × 1 for surface calculations. The Ni_3N surface was modeled using a six-layer slab cut from the optimized bulk structure, with the bottom three layers fixed at their bulk positions and the top three layers allowed to relax. The Ni@Ni_3N interface was constructed by placing a four-layer Ni_3N slab on a four-layer Ni(111) slab, with the bottom two Ni layers fixed. A vacuum region of 20 Å was introduced along the z-direction to avoid spurious interactions between periodic images. During structural relaxation, all atomic positions were fully optimized until the total energy change and the residual forces on each atom were $<10^{-5}$ eV and 0.05 eV/Å, respectively. Zero-point energy (ZPE) and entropy (TS) corrections were obtained from vibrational frequency calculations using the harmonic approximation. The values for each adsorbed intermediate are listed in Table S2. All calculations were performed in vacuum without explicit solvent or applied potential. The free energies reported here are therefore used for qualitative comparison between surfaces rather than quantitative prediction of catalytic activity.

Generally, Gibbs free energy (G) is defined by the following formula:

$$G = E + E_{ZPE} - TS \quad (4)$$

where E, E_{ZPE} and S represent the total energy of adsorption system, zero-point energy and entropy of elementary reaction, respectively [31].

According to the alkaline HER process in Eqs. (5)–(8), the Gibbs free energy change (ΔG) of each step can be obtained by formulas (9–11):

$$* + H_2O + e^- \rightarrow *H_2O + e^- \quad (5)$$

$$*H_2O + e^- \rightarrow *(H-OH) + e^- \quad (6)$$

$$*(H-OH) + e^- \rightarrow *H + OH^- \quad (7)$$

$$*H + OH^- \rightarrow * + 1/2H_2 + OH^- \quad (8)$$

$$\Delta G_1 = G_{*H_2O} - G_* - G_{H_2O} \quad (9)$$

$$\Delta G_2 = G_{*(H-OH)} - G_{*H_2O} \quad (10)$$

$$\Delta G_3 = G_{*H} + G_{OH^-} - G_{*(H-OH)} \quad (11)$$

$$\Delta G_4 = 0.83 - \Delta G_1 - \Delta G_2 - \Delta G_3 \quad (12)$$

in which G_{H_2O}, $G_{*(H—OH)}$ and G_{*H} are Gibbs free energies of adsorbed surfaces by H_2O, (H—OH) and H species, respectively. And G_* is Gibbs free energy of catalyst without adsorbed intermediates [32,33].

3. Results and discussion

3.1. Phase and microstructure analysis

After cleaning and drying, the NF was loaded into a homemade physical vapor ion beam deposition system, where nickel nitride was generated on the NF surface via plasma-assisted nitridation, as schematically illustrated in Fig. 1. As revealed by the SEM images in Fig. 2(a-c), the pristine NF exhibits a relatively smooth surface with clearly discernible grain boundaries. When a bias voltage of −250 V is applied, irregular nanoparticles begin to emerge preferentially along the grain boundaries. This behavior may be attributed to the higher density of defects (e.g., dislocations and vacancies) and elevated interfacial energy at the grain boundaries, which facilitate atomic diffusion and favor the initiation of solid-state phase transformation, thereby leading to a higher nucleation rate in these regions [34]. Upon increasing the bias voltage to −500 V and −750 V, a well-defined, closely packed columnar architecture develops across the NF surface. Notably, the sample treated at −500 V exhibits the most compact morphology, which is expected to effectively enlarge the electrochemically active surface area and enhance the interfacial contact between the electrode and the electrolyte. The nitrogen content of the sample at −500 V bias is up to 9.29 %, and the nitrogen content at −250 V and −750 V bias is 2.04 % and 4.67 %, respectively (Fig. S1, supporting information). The observed bias-dependent morphological evolution can be understood from the competition between nitrogen ion implantation and surface sputtering. At low bias (−250 V), the kinetic energy of nitrogen ions is insufficient to overcome the surface barrier and efficiently break the N≡N bond, resulting in limited nitridation and nanoparticle nucleation preferentially at defect-rich grain boundaries. At moderate bias (−500 V), the ion energy is sufficient to promote nitrogen incorporation while minimizing excessive sputtering, leading to dense and uniform nanocolumn growth. The formation of the nanocolumns can be attributed to the combined effects of preferential nitridation at high-energy surface sites, shadowing-induced anisotropic growth, and ion-enhanced surface diffusion. Initially, nitridation occurs preferentially at defect-rich or high-energy sites, creating local protrusions. These protrusions then receive a higher ion flux than the surrounding recessed areas, while the recessed regions are partially shadowed from direct ion bombardment [35]. This shadowing effect promotes continued vertical growth of the protrusions, eventually developing them into columnar structures. Meanwhile, ion bombardment enhances the surface mobility of adsorbed species, allowing the column sidewalls to remain relatively smooth and well separated. Further increasing the bias to −750 V causes

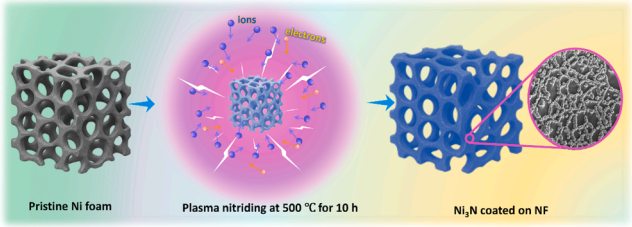

Fig. 1. The schematic of preparation process for the Ni_3N/NF.

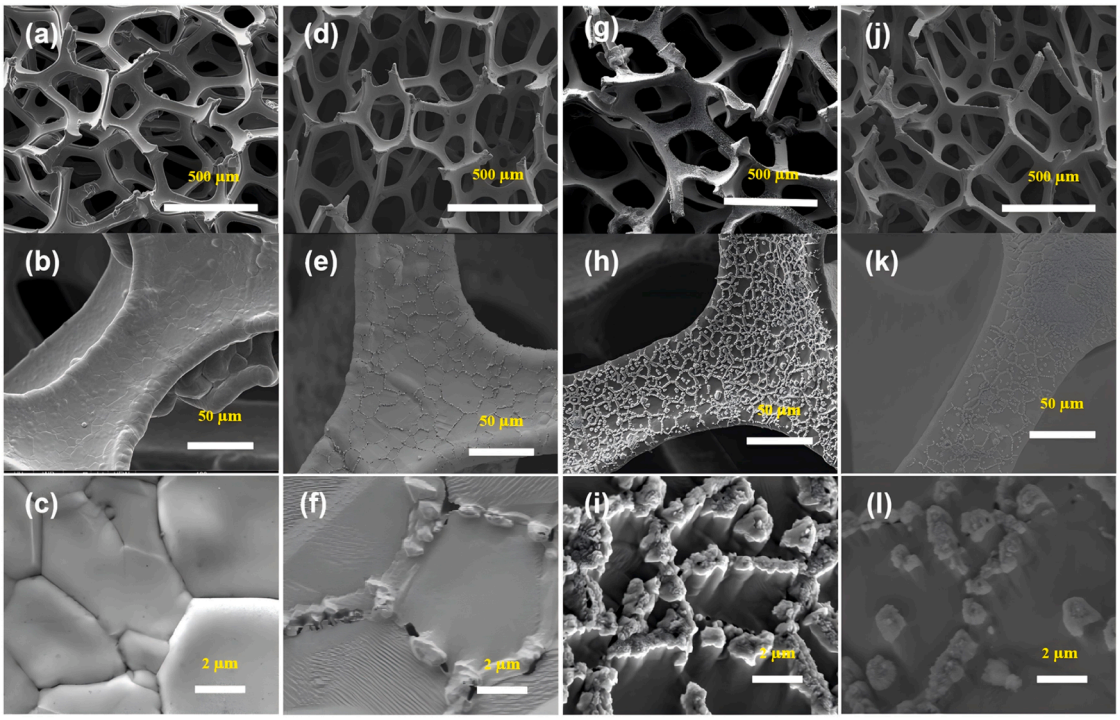

Fig. 2. SEM characterization of NF (a-c) and NF-250 (d-f), NF-500 (g-i), NF-750 (j-l).

high-energy ion bombardment to re-sputter nitrogen atoms from the surface, reducing the nitrogen content and disrupting columnar uniformity. This trend is consistent with previous studies on plasma nitriding of metallic surfaces and highlights the unique capability of bias control in tailoring the self-assembly of Ni_3N nanostructures directly on Ni foam [36].

XRD patterns were also collected for the pristine NF and nitrided samples (Fig. S2). Only diffraction peaks corresponding to metallic Ni were observed, with no distinct Ni_3N peaks detectable. This is not unexpected, because the nitride shell is only approximately 50–80 nm thick and is supported on a strongly diffracting Ni substrate, making it difficult to detect by conventional laboratory XRD. In addition, the Ni_3N phase formed under low-temperature plasma conditions may be partially nanocrystalline or poorly ordered, further reducing its XRD visibility. In order to study the columnar components grown on the surface of nickel foam, the samples were tested by XPS, as shown in Fig. 3(a) and (b). In the 2p spectrum of Ni, the binding energy at 852.9 eV and 870.3 eV corresponds to the bonding of Ni-N, the binding energy at 855.8 eV and 873.8 eV corresponds to the peak position of Ni-based, and the binding energy at 861.4 eV and 879.5 eV corresponds to the two accompanying peaks of Ni [37,38]. In the 1 s spectrum of N, the peak at 397.8 eV corresponds to the typical N-Ni bond [39].

In order to further study the microstructure of the prepared electrode, HRTEM analysis was performed on the NF-500 sample. From the distribution map of nitrogen elements in Fig. 4(a) and (b), it can be observed that the content of N elements gradually decreases from the outside to the inside, and the element distribution in the line scan diagram further confirms this result. The Ni_3N shell thickness was estimated by measuring the distance from the outer surface to the Ni/Ni_3N interface at multiple positions along the same nanocolumn. The measured values fall within the range of approximately 50–80 nm. As shown in Fig. 4(c), the lattice spacings corresponding to the (220), (200), and (111) planes of nickel are clearly visible in the HRTEM image, with values of 0.126, 0.177, and 0.204 nm, respectively. The lattice spacings of 0.214 nm and 0.204 nm correspond to the (002) and (111) planes of Ni_3N, respectively. In addition, the diffraction rings of Ni_3N (110) and (111) are depicted by the selected area electron diffraction pattern in Fig. 4(d), which proves that the generated Ni_3N is consistent with the XPS results.

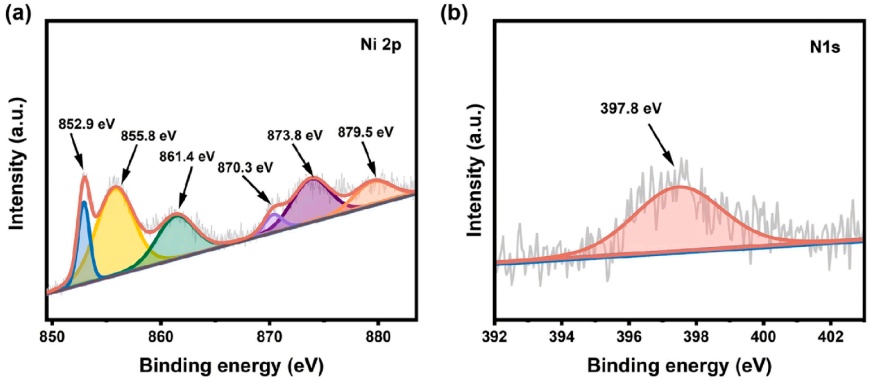

Fig. 3. XPS spectra of NF-500 sample (a) Ni 2p; (b) N 1 s.

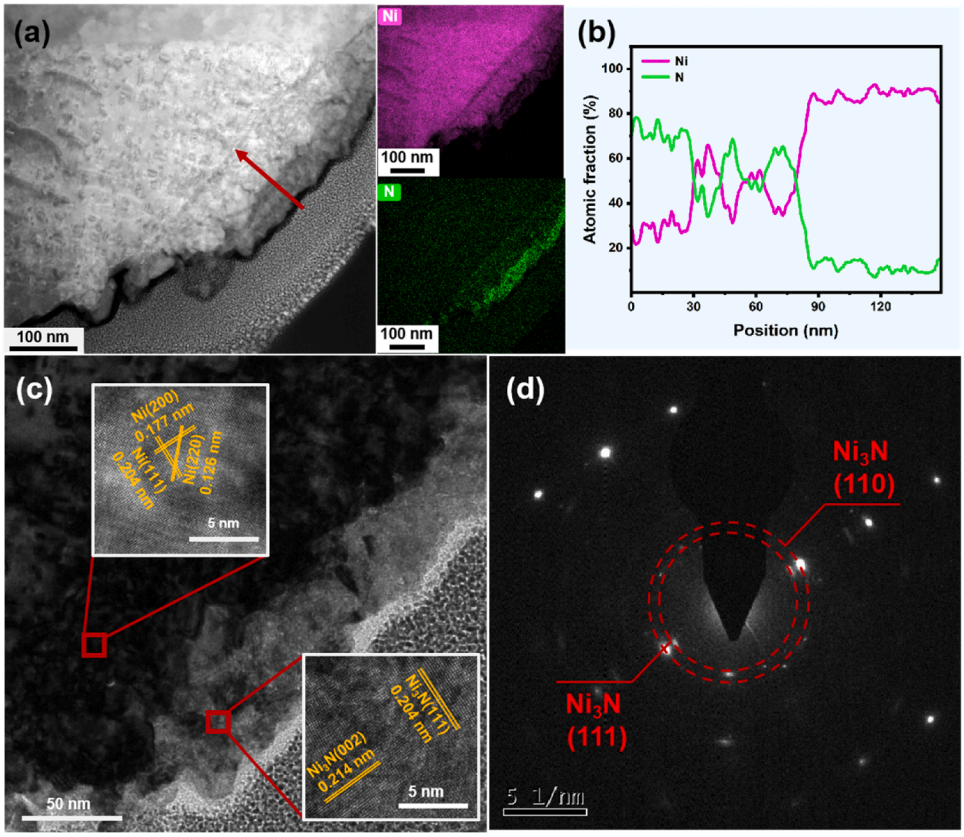

Fig. 4. TEM characterization of NF-500 sample (a) HAADF image and corresponding EDS mappings; (b) Line scan element distribution map; (c) HRTEM images; (d) SAED pattern.

3.2. Electrocatalytic HER performance analysis

The standard three-electrode workstation was used to evaluate the HER activity of the modified nickel foam electrode in 1.0 M KOH solution under different bias voltages, as shown in Fig. 5. The LSV polarization curves of the modified nickel foam electrode in 1 M KOH electrolyte under different bias voltages are shown in Fig. 5(a), which is illustrated by the change of overpotential (η_{10} and η_{20}) at current densities of 10 and 20 mA/cm^2. At the same current density, the lower the overpotential, the higher the electrode activity. It can be seen from the figure that the NF-500 sample exhibits the lowest overpotential $\eta_{10} = 64$ mV and $\eta_{20} = 111$ mV, which is much lower than that of pure NF ($\eta_{10} = 174$ mV, $\eta_{20} = 221$ mV), NF-250 ($\eta_{10} = 111$ mV, $\eta_{20} = 169$ mV) and NF-750 ($\eta_{10} = 83$ mV, $\eta_{20} = 139$ mV). Compared with the previously reported nickel-based catalysts (Table S1, Supporting Information) [40–51]. It should be noted that the overpotential of NF-500 (64 mV at 10 mA cm^{-2}) is not the lowest among all reported Ni-based catalysts; several binary or heterostructured systems achieve lower values. Nevertheless, NF-500 remains within the competitive range for self-supported Ni_3N-based electrodes, and its Tafel slope of 36 mV dec^{-1} is among the lower reported values, indicating favorable kinetics. On the one hand, the improved performance is attributed to nitrogen incorporation into the nickel lattice during plasma nitriding, which modulates the d-orbital electron density and optimizes the hydrogen adsorption free energy (ΔG_{H^*}), thereby enhancing the intrinsic catalytic activity [52]. On the other hand, the surface of the sample after nitriding at −500 V bias voltage grows obvious columnar morphology, which increases the specific surface area of the electrode and exposes more active

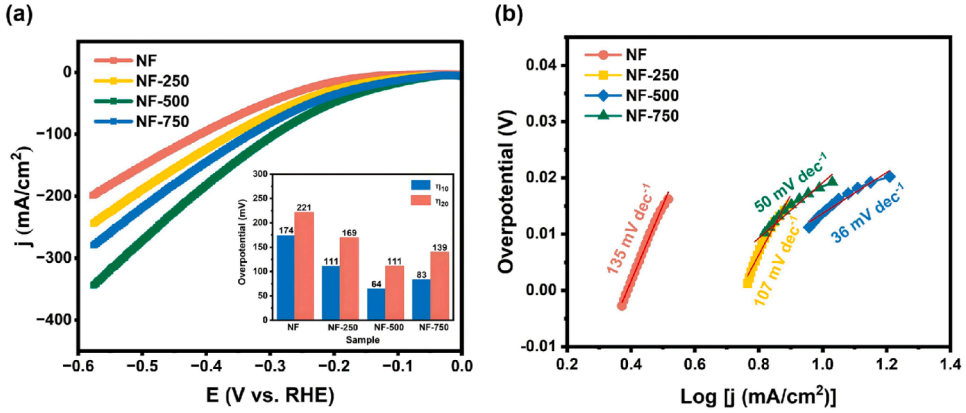

Fig. 5. The electrochemical parameters of NF, NF-250, NF-500 and NF-750 in 1.0 M KOH, (a) LSV curve, the overpotential required for η10 and η20, (b) Tafel slope.

sites. However, the present data cannot completely exclude possible contributions from plasma-induced surface cleaning, defect generation, or thermal annealing. Dedicated control experiments would be required to quantitatively separate these factors, which we identify as a direction for future work. And the electrochemical active area of the samples was tested. The CV scanning results are presented in Fig. 6(a-d). The double-layer capacitance (C_{dl}) values of all samples were derived from the CV measurements, as shown in Fig. 7(a). The calculated electrochemical active surface areas for NF, NF-250, NF-500, and NF-750 were 2.5, 13.75, 52.5, and 37.25 cm^2, respectively. The significantly increased ECSA of NF-500 is closely associated with the formation of nanocolumn arrays on the nickel foam substrate, which expose more catalytically accessible surface sites. It should be noted that the C_{dl} values were measured in 0.1 M NaOH, while the HER performance was evaluated in 1 M KOH, and a generic specific capacitance of 0.04 mF cm^{-2} was used. These factors introduce uncertainty into the absolute ECSA values and limit the reliability of quantitative ECSA-normalized activity comparisons. The calculated ECSA values are used only for qualitative comparison among samples prepared under identical conditions, rather than for absolute quantification of intrinsic active surface area. Moreover, the in-situ growth of Ni_3N on nickel foam establishes intimate interfacial contact between the active phase and conductive substrate, thereby facilitating interfacial charge-transfer processes during HER. Unlike conventional powder catalysts requiring polymer binders, the self-supported electrode configuration avoids possible blockage of active sites and minimizes additional charge-transfer resistance [53]. The columnar Ni_3N structures expose a larger accessible surface area, as indicated by the increased ECSA. The enhanced activity is therefore attributed to the overall increase in accessible surface area and the interfacial electronic modulation.

Fig. 5(b) shows the Tafel slope of each sample, which is used as an important parameter to evaluate the catalytic activity reaction mechanism. It is used to describe the kinetic characteristics of the reaction and can directly reflect the intrinsic activity of the material. The NF-500 electrode exhibits a Tafel slope of 36 mV dec^{-1}, lower than those of NF (135 mV dec^{-1}), NF-250 (107 mV dec^{-1}), and NF-750 (50 mV dec^{-1}), indicating faster HER kinetics, which is consistent with the polarization curve results. In addition, according to the literature, the hydrogen evolution path on the surface of the catalytic material can be determined by the Tafel slope value. The hydrogen evolution reaction is a process in which protons (H^+) or water molecules receive electrons on the cathode surface and are reduced to hydrogen in electrochemistry. The reaction is more difficult under alkaline conditions or neutral conditions, because H^+ mainly comes from the formation of ($2H_2O + 2e^- \rightarrow H_2 + 2OH^-$) after electrolysis of water. It is usually divided into two elementary reactions. One is the Volmer step: H_2O adsorbs on the surface of the catalyst and accepts electrons to form an adsorbed H* ($H_2O + e^- \rightarrow H^* + OH^-$); the second is the Tafel or Heyrovsky step, that is, two adsorbed hydrogens combine to form hydrogen ($2H^* \rightarrow H_2$) or the adsorbed hydrogen reacts with H_2O in the solution to form hydrogen ($H^* + H_2O +$

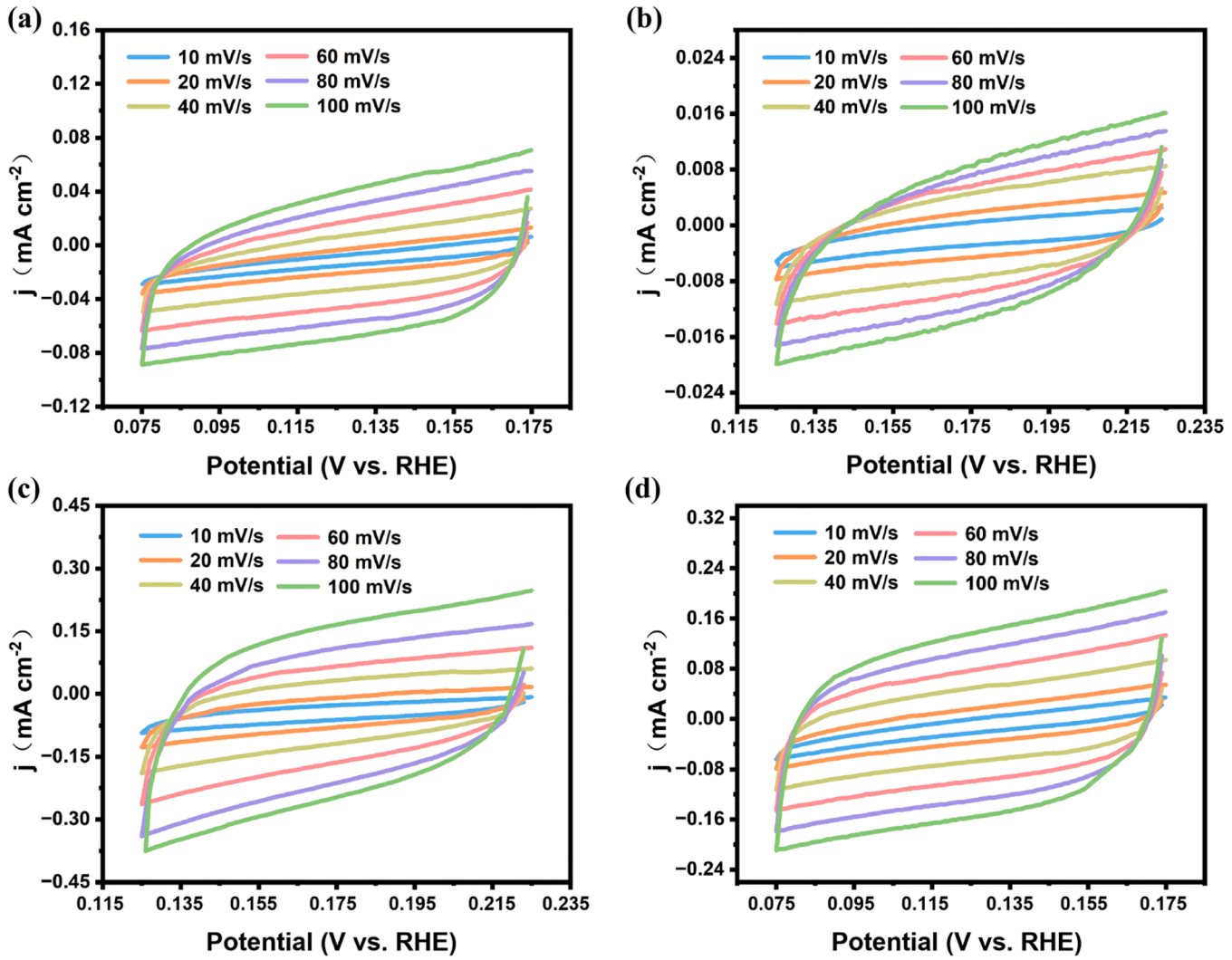

Fig. 6. ECSV curves used to determine C_{dl} of (a) NF, (b) NF-250, (c) NF-500, and (d) NF-750.

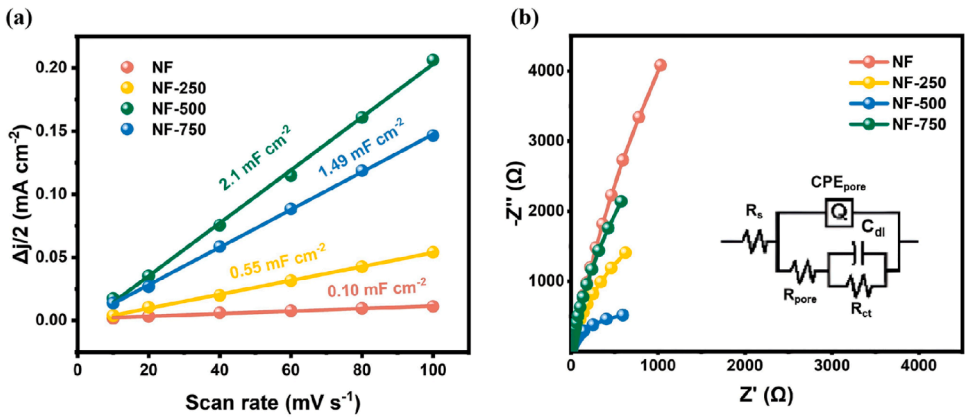

Fig. 7. (a) C_{dl} estimated by plotting current density changes; (b) Nyquist diagram of NF, NF-250, NF-500 and NF-750, where the illustration is the equivalent circuit model.

$e^- \rightarrow H_2 + OH^-$). From the Tafel value, it can be determined that the hydrogen evolution path on the surface of the catalytic material is the Volmer-Heyrovsky step. The rate-limiting step of the pure NF sample is the Volmer reaction (> 120 mV dec^{-1}), and the rate-limiting step of others is the Heyrovsky reaction (30–120 mV dec^{-1}) [54,55].

We performed electrochemical impedance spectroscopy (EIS) to characterize the charge transfer resistance during electrochemical reactions. The Nyquist plots in Fig. 7(b) clearly demonstrate the facilitated charge transfer between the electrode material and electrolyte interface. The illustrations are equivalent circuit models, including R_s (solution resistance), R_{pore} (pore resistance), CPE_{pore} (constant phase element), R_{ct} (charge transfer resistance), C_{dl} (double layer capacitance), and the fitting results are shown in Table 1. The R_{ct} of NF, NF-250, NF-500 and NF-750 were 28,360, 6264, 1217 and 20,940 Ω, respectively. We can see that the R_{ct} values of the samples after nitriding are reduced, which indicates that the charge transfer efficiency on the electrode surface is improved after plasma nitriding. Among these, the NF-500 sample exhibits the smallest charge transfer resistance, indicating rapid charge transfer at the Ni_3N/NF-electrolyte interface. The reduced electrochemical impedance is beneficial for accelerated HER kinetics. Efficient bubble release behavior represents a critical yet often overlooked factor governing the performance of hydrogen evolution electrodes [56]. The vertically aligned nanocolumn architecture with nanoscale intercolumnar gaps may facilitate the release of H_2 bubbles and reduce active-site blockage [57]. This is proposed as a possible morphological advantage. The stability of sample NF-500 was evaluated in 1 M KOH solution. Under potentiostatic conditions at a current density of 10 mA cm^{-2}, no decay in current density was observed after 72 h of operation, suggested that the electrode maintains its electrochemical activity under continuous operation. In addition, a step stability test involving alternating current densities of 10 and 100 mA cm^{-2} revealed a slight performance degradation after 24 h of continuous operation (Fig. 8(a), (b)). To examine the structural and chemical stability of the electrode after prolonged HER, post-reaction characterization was performed on NF-500 after the 72 h chronoamperometric test. As shown in Figure S3, the vertically aligned nanocolumn morphology is well preserved, with no obvious detachment or collapse. The XPS spectra of the post-reaction electrode (Figure S4a, b) still exhibit clear Ni-N bonding features in both the Ni 2p and N 1 s regions, confirming that the Ni_3N phase is largely retained. Compared with the as-prepared sample, the peaks are slightly shifted to lower binding energies, which is attributed to the partial reduction of surface oxide/hydroxide species under prolonged cathodic polarization. These results indicate that the active architecture is structurally and chemically stable over the tested duration, consistent with the negligible current decay observed in the stability test. These results indicate acceptable short-term stability under the tested conditions. However, it should be noted that Faradaic efficiency was not measured, and the stability at high current densities was only evaluated for a limited duration. Further work is needed to fully assess long-term durability under industrially relevant conditions (Table 2).

3.3. Theoretical analysis

The aforementioned experimental results indicate that the hydrogen evolution reaction (HER) catalytic activity of the electrode is significantly enhanced after vacuum plasma nitriding treatment. Numerous studies have confirmed that nickel nitride (Ni_3N) possesses favorable HER catalytic performance. To gain deeper insight into the performance enhancement mechanism observed experimentally and to better align with actual catalytic environments, this study constructed models of pure Ni_3N and the metal-nitride interface structure Ni@Ni_3N to simulate surface reaction behavior during the alkaline HER process.

In alkaline media, the HER typically follows a two-step mechanism: the first step is the Volmer step, involving the dissociation of a water molecule to form a co-adsorbed *(H-OH) intermediate; this is followed by either the Heyrovsky step or the Tafel step, where *H recombination occurs to release H_2. Therefore, the key reaction intermediates in alkaline HER mainly include *H_2O, *(H-OH), and *H. Among these, the adsorption configuration of *(H-OH) directly influences subsequent reaction pathways, necessitating first the identification of a stable adsorption site for *OH, followed by investigation of *H adsorption behavior.

We first examined possible adsorption sites for H_2O molecules on the pure Ni_3N surface (Fig. S5 a-l). After structural optimization, the system at site 3 exhibited the lowest total energy (E = −405.82 eV), indicating that this configuration is the most thermodynamically stable state and

Table 1
Fitting values of electronic elements from equivalent circuit model.

Sample	R_s (Ω)	CPE_{pore} (mF/cm^2)	n_{pore}	R_{pore} (Ω)	C_{dl} (mF/cm^2)	R_{ct} (Ω)
NF	0.986	1.302×10^{-3}	0.8799	1.8	1.98×10^{-3}	28,360
NF-250	0.835	5.711×10^{-3}	0.8752	19.16	1.753×10^{-3}	6264
NF-500	0.8017	6.563×10^{-3}	0.8608	19.91	1.474×10^{-3}	1217
NF-750	0.9615	4.252×10^{-3}	0.8876	21.89	1.343×10^{-3}	20,940

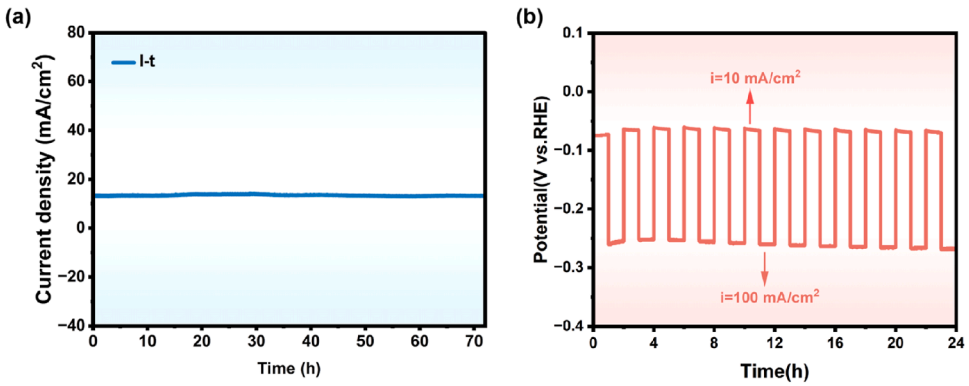

Fig. 8. Stability test of NF-500 sample (a) Chronoamperometric current curve; (b) Step potential test.

Table 2
Calculated Cdl and ECSA values of catalysts.

Sample	C_{dl} (mF)	Cs (mF cm^{-2})	ECSA (cm^2)
NF	0.1	0.04	2.5
NF-250	0.55	0.04	13.75
NF-500	2.1	0.04	52.5
NF-750	1.49	0.04	37.25

corresponds to the optimal adsorption site for water molecules. On this basis, the adsorption of *OH was further investigated (Fig. S6), and configurations suitable for subsequent *H adsorption were screened (Fig. S7), ultimately enabling the modeling of co-adsorbed *(H-OH). In the configuration selection, the distance between *OH and *H must be kept moderate to avoid premature separation or direct recombination. Following this principle, *(H-OH) and *H tend to adsorb at site 2 (Fig. S7) and site 4 (Fig. S8) on pure Ni_3N. For the Ni@Ni_3N model, the method for determining intermediate adsorption sites is similar (Fig. S9-S12).

Based on equations (9-12), we systematically calculated the Gibbs free energy changes for each elementary reaction on the surfaces of the two catalysts; the results are summarized in Fig. 9(c), (d). For pristine Ni_3N, the calculated values are $\Delta G_1 = -0.36$ eV, $\Delta G_2 = -0.54$ eV, $\Delta G_3 = 1.29$ eV, and $\Delta G_4 = 0.44$ eV. For Ni@Ni_3N, the corresponding values are $\Delta G_1 = -0.06$ eV, $\Delta G_2 = -0.90$ eV, $\Delta G_3 = 0.97$ eV, and $\Delta G_4 = 0.83$ eV. The step with the largest positive ΔG is ΔG_3, which corresponds to the formation of *H from the co-adsorbed (H—OH) intermediate. On Ni@Ni_3N, ΔG_3 is 0.97 eV, which is 0.32 eV lower than the value of 1.29 eV on pristine Ni_3N. It should be emphasized that ΔG_3 is not the conventional hydrogen adsorption free energy (ΔG_{H^*}) referenced to gaseous H_2; it is the free-energy change for the specific elementary step *(H—OH)+ e^- → H + OH^- evaluated using the computational hydrogen electrode reference. Therefore, the absolute value of ΔG_3 should not be compared with the ideal ΔG_{H^*} of 0 eV. The key finding is the relative decrease of ΔG_3 on Ni@Ni_3N, which indicates that the interface facilitates this thermodynamically least favorable step compared with pure Ni_3N, consistent with the enhanced HER activity observed experimentally. It should be noted that the calculated ΔG values represent thermodynamic free-energy differences between the initial and final states of each elementary step. No transition-state calculations were performed, and therefore activation barriers were not obtained. Accordingly, the step with the largest positive ΔG is referred to as the thermodynamically least favorable step, rather than the rate-determining step.

As shown in Fig. 10, pristine Ni_3N exhibits electronic states mainly distributed below the Fermi level, with pronounced density of states (DOS) peaks in the energy range of approximately −5 to −1 eV, whereas the DOS near the Fermi level is relatively weak. In contrast, Ni@Ni_3N displays a broader and more continuous DOS distribution around the Fermi level within −1 to +1 eV, indicating an increased availability of electronic states in the reaction-relevant energy region. This result suggests that the introduction of metallic Ni induces interfacial electronic reconstruction at the Ni/Ni_3N heterointerface, leading to redistribution of electronic states toward the Fermi level. Since electronic states near the Fermi level play a critical role in interfacial charge-transfer kinetics during electrocatalysis, the enhanced DOS around the Fermi level in Ni@Ni_3N is expected to facilitate electron transport and charge injection to catalytic active sites, thereby promoting alkaline HER kinetics. It should be noted that the DFT calculations in this work model idealized Ni_3N and Ni@Ni_3N surfaces under vacuum conditions. The real electrode surface is more complex and may contain metallic Ni regions, the nitride phase, surface oxide/hydroxide species, and potentially reconstructed phases under alkaline HER conditions. The surface composition may further evolve upon immersion in the alkaline electrolyte and under cathodic polarization. Therefore, the theoretical results should be interpreted as a qualitative indication that the Ni/Ni_3N interface may facilitate the key elementary steps, rather than as a quantitative description of the actual catalytic surface. A more complete understanding would require modeling the surface oxide/hydroxide species and the electrochemical environment.

4. Conclusions

In summary, a robust columnar-structured Ni_3N electrocatalyst has been successfully fabricated on nickel foam via a facile and scalable vacuum plasma nitridation strategy. The resulting electrode features vertically aligned nanocolumns with well-defined interfacial regions, providing abundant accessible active sites and efficient mass and charge transport pathways. Benefiting from this vertically aligned nanocolumn architecture and optimized electronic structure, the Ni_3N/NF electrode demonstrates improved alkaline HER activity, achieving an overpotential of 64 mV at 10 mA cm^{-2}, a small Tafel slope of 36 mV dec^{-1}, and acceptable short-term operational stability under the tested conditions. DFT calculations reveal that the interfacial Ni@Ni_3N region formed during plasma nitridation modulates the hydrogen adsorption free energy, thereby enhancing the intrinsic catalytic activity. Combined experimental and theoretical analyses demonstrate that the optimized HER performance can be attributed to the synergistic effects between the atomic-level electronic structure modulation and the nano-scale architectural advantages, where the former optimizes the adsorption/desorption behavior of reaction intermediates while the latter facilitates charge transfer and bubble release. This work not only presents a non-precious metal electrocatalyst but also provides mechanistic insight into the rational design of transition metal nitride-based materials for sustainable energy conversion applications.

Supporting Information

Supporting Information is available from the Wiley Online Library or from the author.

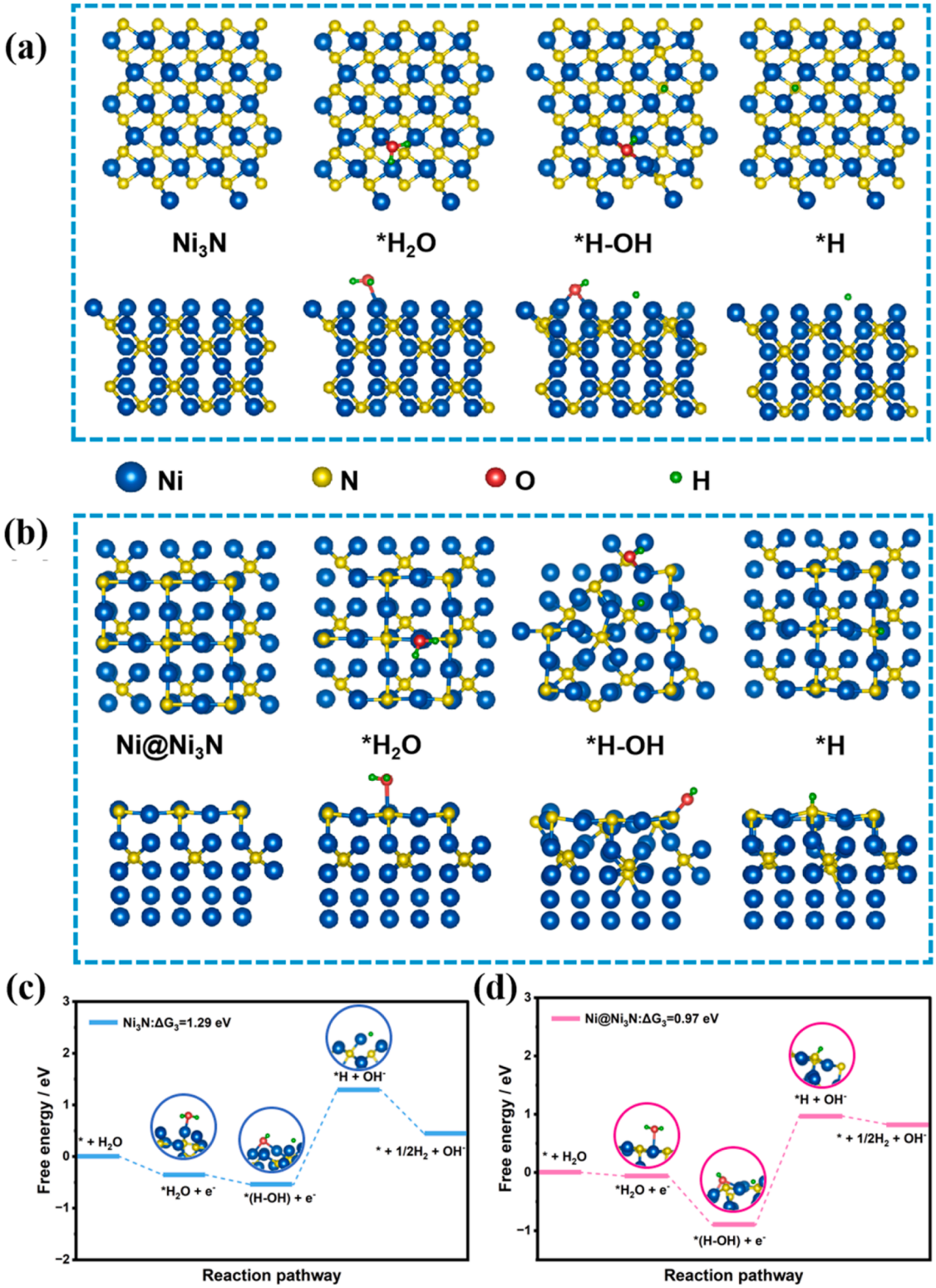

Fig. 9. Top and side view of $*H_2O$, *(H—OH) and *H intermediates adsorbed on (a)Ni_3N, (b) Ni@Ni_3N; Gibbs free energy diagrams of (c) Ni_3N and (d) Ni@Ni_3N.

CRediT authorship contribution statement

Xueqing Zhao: Writing – original draft, Software, Investigation, Formal analysis, Data curation, Conceptualization. **Mei Wang:** Software, Data curation, Conceptualization. **Caifeng Zhang:** Writing – original draft, Methodology, Investigation. **Sixie Zhang:** Writing – review & editing, Supervision, Conceptualization. **Guanshui Ma:** Writing – review & editing, Validation, Supervision, Conceptualization. **Aiying Wang:** Writing – review & editing, Supervision, Methodology, Funding acquisition, Conceptualization.

Declaration of competing interest

The authors declare that they have no known competing financial

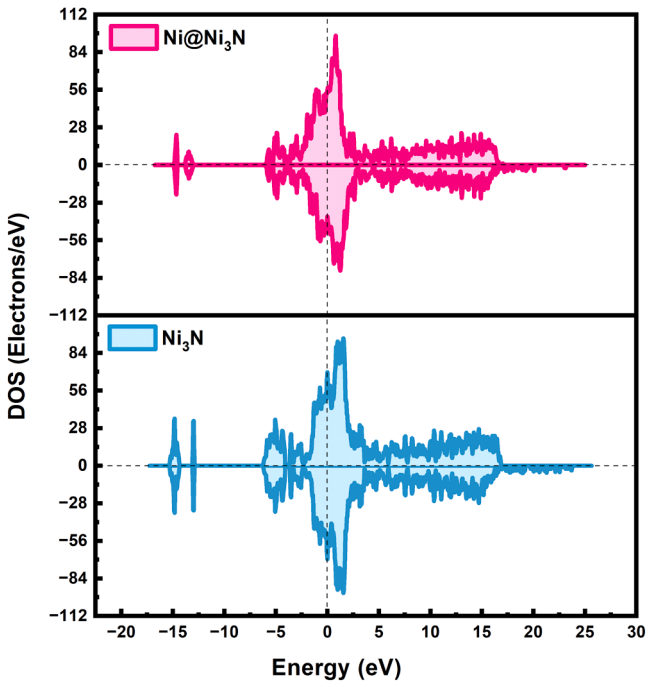

Fig. 10. Electronic density of states of Ni_3N and Ni@Ni_3N.

interests or personal relationships that could have appeared to influence the work reported in this paper.

Acknowledgements

This work was financially supported the Zhejiang Provincial Natural Science Foundation of China (No. LD24E010003), Key Research and Development Program of Ningbo (2025Z135), the Open Research Fund of the State Key Laboratory of Tropic Ocean Engineering Materials and Materials Evaluation (No. STOEM2025KF003).

Supplementary materials

Supplementary material associated with this article can be found, in the online version, at doi:10.1016/j.electacta.2026.149943.

Data availability

Data will be made available on request.

References

[1] V. Tharun, P.S. Kumar, A comprehensive review on hydrogen production, purification, storage, and utilization: challenges and future directions, Renew. Sustain. Energy Rev. 224 (2025) 116067, https://doi.org/10.1016/j.rser.2025.116067.
[2] C. Tang, Y. Chen, J. Rao, H. Guo, Y. Zhou, Solar-to-hydrogen conversion efficiency for photovoltaic water electrolysis to produce green hydrogen, Small 21 (29) (2025) 2502342, https://doi.org/10.1002/smll.202502342.
[3] Y. Li, J. Guo, R. Wang, Y. Zhao, Q. Wang, J. Li, T. Ling, Design of RuO_x electrocatalysts containing metallic Ru on the surface to accelerate the alkaline hydrogen evolution reaction, ACS Appl. Mater. Interfaces 17 (5) (2025) 7784–7792, https://doi.org/10.1021/acsami.4c19204.
[4] B. Azizimehr, T. Armaghani, R. Ghasemiasl, A.K. Nejadian, M.A. Javadi, A comprehensive review of recent developments in hydrogen production methods using a new parameter, Int. J. Hydrog. Energy 72 (2024) 716–729, https://doi.org/10.1016/j.ijhydene.2024.05.219.
[5] W. Chen, T. Li, Y. Ren, J. Wang, H. Chen, Q. Wang, Biological hydrogen with industrial potential: improvement and prospection in biohydrogen production, J. Clean. Prod. 387 (2023) 135777, https://doi.org/10.1016/j.jclepro.2022.135777.
[6] H. Sun, X. Xu, H. Kim, W. Jung, W. Zhou, Z. Shao, Electrochemical water splitting: bridging the gaps between fundamental research and industrial applications, Energy Env. Mater. 6 (2023) e12441, https://doi.org/10.1002/eem2.12441.
[7] Z. Yu, Y. Duan, X. Feng, X. Yu, M. Gao, S. Yu, Clean and affordable hydrogen fuel from alkaline water splitting: past, recent progress, and future prospects, Adv. Mater. 33 (2021) 2007100, https://doi.org/10.1002/adma.202007100.
[8] L. Liu, Y. Wang, Y. Zhao, Y. Wang, Z. Zhang, T. Wu, W. Qin, S. Liu, B. Jia, H. Wu, D. Zhang, X. Qu, M. Chhowalla, M. Qin, Ultrahigh Pt-mass-activity hydrogen evolution catalyst electrodeposited from bulk Pt, Adv. Funct. Mater. 32 (20) (2022) 2112207, https://doi.org/10.1002/adfm.202112207.
[9] X. Gao, Q. Guo, S. Zhang, Y. Jiang, C. Ji, W. Zhang, M. Zheng, B. Yu, D. Wang, Y. Fan, F. Zheng, W. Chen, Regulating the protecting ligand content on Pt cluster surface for highly efficient electrocatalytic hydrogen evolution reaction, Appl. Surf. Sci. 703 (2025) 163129, https://doi.org/10.1016/j.apsusc.2025.163129.
[10] D. Mohapatra, M.Z. Ansari, Y. Son, S. Lee, Y. Kang, S.-H. Kim, Precious metal Ir-ALD process engineered 2D V-MXene advanced heterostructures for next-generation hydrogen evolution electrocatalyst, Mater. Today Nano 29 (2025) 100557, https://doi.org/10.1016/j.mtnano.2024.100557.
[11] C. Wang, W. Guo, T. Chen, W. Lu, Z. Song, C. Yan, Y. Feng, F. Gao, X. Zhang, Y. Rao, L. Qian, S. Xu, G. Huang, Y. Zheng, W. Yan, J. Zhang, Advanced noble-metal/transition-metal/metal-free electrocatalysts for hydrogen evolution reaction in water-electrolysis for hydrogen production, Coord. Chem. Rev. 514 (2024) 215899, https://doi.org/10.1016/j.ccr.2024.215899.
[12] J. Jiang, Y. Qiu, H. Dong, L. Yang, Y. Miao, L. Xiong, B. Gao, X. Zhang, P.K. Chu, X. Peng, Enhancing hydrogen evolution by heterointerface engineering of Ni/MoN catalysts, J. Colloid Interface Sci. 686 (2025) 681–690, https://doi.org/10.1016/j.jcis.2025.01.201.
[13] A.A. Feidenhans'l, Y.N. Regmi, C. Wei, D. Xia, J. Kibsgaard, L.A. King, Precious metal free hydrogen evolution catalyst design and application, Chem. Rev. 124 (9) (2024) 5617–5667, https://doi.org/10.1021/acs.chemrev.3c00712.
[14] X. Chen, H. Liu, A. Jiang, X. Li, J. Xiao, Highly efficient electrocatalytic hydrogen evolution by double-shelled hollow spheres with Mo_2C/C heterostructure, Appl. Surf. Sci. 695 (2025) 162869, https://doi.org/10.1016/j.apsusc.2025.162869.
[15] X. Yin, Y. Wang, X. Fu, X. Liu, Y. Wang, Z. Liu, Reversible hydrogen spillover enhances hydrogen evolution reaction on electrodeposited $MoNi_4/Ni_{17}W_3$ with amorphous/crystalline heterostructure, J. Power Sources 641 (2025) 236912, https://doi.org/10.1016/j.jpowsour.2025.236912.
[16] W. Zhang, N. Han, J. Luo, X. Han, S. Feng, W. Guo, S. Xie, Z. Zhou, P. Subramanian, K. Wan, J. Arbiol, C. Zhang, S. Liu, M. Xu, X. Zhang, J. Fransaer, Critical role of phosphorus in hollow structures cobalt-based phosphides as bifunctional catalysts for water splitting, Small 18 (4) (2022) 2103561, https://doi.org/10.1002/smll.202103561.
[17] Y. Zhao, J. Zhang, Y. Xie, B. Sun, J. Jiang, W. Jiang, S. Xi, H. Yang, K. Yan, S. Wang, X. Guo, P. Li, Z. Han, X. Lu, H. Liu, G. Wang, Constructing atomic heterometallic sites in ultrathin nickel incorporated cobalt phosphide nanosheets via a boron-assisted strategy for highly efficient water splitting, Nano Lett. 21 (1) (2021) 823–832, https://doi.org/10.1021/acs.nanolett.0c04569.
[18] K. Wu, Y. Meng, J. Xu, K. Edalati, H. Shao, W. Li, H.-J. Lin, Novel Fe-based nanoglass as efficient noble-metal-free electrocatalyst for alkaline hydrogen evolution reaction, Scr. Mater. 21 (2021) 823–832, https://doi.org/10.1021/acs.nanolett.0c04569.
[19] D.Y. Li, L.L. Liao, H.Q. Zhou, Y. Zhao, F.M. Cai, J.S. Zeng, F. Liu, H. Wu, D.S. Tang, F. Yu, Highly active non-noble electrocatalyst from Co_2P/Ni_2P nanohybrids for pH-universal hydrogen evolution reaction, Mater. Today Phys. 16 (2021) 100314, https://doi.org/10.1016/j.mtphys.2020.100314.
[20] L. Xie, Y. Dong, H. Ling, Z. Xiang, B. Long, J. Wang, L. Zhao, X. Zhou, W. He, X. Zheng, Balancing hydrogen adsorption/desorption on MoS_2 by Co, V dual-doping for efficient hydrogen evolution reaction, Appl. Surf. Sci. 720 (2026) 165147, https://doi.org/10.1016/j.apsusc.2025.165147.
[21] M. Ligier, K. Ciurzyńska, A. Ilnicka, M. Szkoda, Transition metal nitrides: synthesis strategies, structural properties, and functional modifications, Coord. Chem. Rev. 564 (2026) 218073, https://doi.org/10.1016/j.ccr.2026.218073.
[22] Z. Yang, H. Xu, T. Shuai, Q. Zhan, Z. Zhang, K. Huang, C. Dai, G. Li, Recent progress in the synthesis of transition metal nitride catalysts and their applications in electrocatalysis, Nanoscale 15 (2023) 11777–11800, https://doi.org/10.1039/D3NR01607B.
[23] Y. Wang, E. Ender, S. Kumar, C. Tseng, G. Yang, B. Ye, C. Liang, Y. Yu, N. West, I. Chauhan, J.H. Ng, S. Halder, S.G. Ji, G. Held, M.P. Ryan, K.L. Moore, A. S. Walton, R.R. Rao, Active phase of nickel electrocatalysts driving alkaline hydrogen evolution, Adv. Mater. (2026) e74591, https://doi.org/10.1002/adma.74591.
[24] G. Wu, X. Han, J. Cai, P. Yin, P. Cui, X. Zheng, H. Li, C. Chen, G. Wang, X. Hong, In-plane strain engineering in ultrathin noble metal nanosheets boosts the intrinsic electrocatalytic hydrogen evolution activity, Nat. Commun. 13 (2022) 4200, https://doi.org/10.1038/s41467-022-31971-4.
[25] S. Niu, J. Wang, Y. Wu, J. Zhang, X. Wu, H. Luo, W.-J. Jiang, Constructing a built-in electric field to accelerate water dissociation for efficient alkaline hydrogen evolution, ACS Appl. Mater. Interfaces 16 (24) (2024) 31480–31488, https://doi.org/10.1021/acsami.4c05604.
[26] G. Ma, Y. Zheng, P. Guo, R. Chen, J. Yuan, J. Yan, L. Cui, A. Wang, Enhancing hydrogen evolution reaction by synergistically coupling NiMo alloy with Mo on Ni foam, J. Alloy. Compd. 933 (2023) 167855, https://doi.org/10.1016/j.jallcom.2022.167855.
[27] C. Xiao, Y. Li, X. Lu, C. Zhao, Bifunctional porous NiFe/$NiCo_2O_4$/Ni foam electrodes with triple hierarchy and double synergies for efficient whole cell water splitting, Adv. Funct. Mater. 26 (2016) 3515–3523, https://doi.org/10.1002/adfm.201505302.

[28] Y. Wei, L. Yi, S. Zhang, C. Ni, X. Cai, W. Sun, W. Hu, Ni-Mo nitride synthesized via mild plasma for efficient alkaline hydrogen evolution electrocatalysis, J. Mater. Chem. A 12 (2024) 8534–8542, https://doi.org/10.1039/D3TA07566D.
[29] G. Li, X. Wu, H. Guo, Y. Guo, H. Chen, Y. Wu, J. Zheng, X. Li, Plasma transforming $Ni(OH)_2$ nanosheets into porous nickel nitride sheets for alkaline hydrogen evolution, ACS Appl. Mater. Interfaces 12 (5) (2020) 7423–7431, https://doi.org/10.1021/acsami.9b19495.
[30] R. Martínez-Hincapié, J. Wegner, M.U. Anwar, A. Raza-Khan, S. Franzka, S. Kleszczynski, V. Čolić, The determination of the electrochemically active surface area and its effects on the electrocatalytic properties of structured nickel electrodes produced by additive manufacturing, Electrochim Acta 476 (2024) 143663, https://doi.org/10.1016/j.electacta.2023.143663.
[31] Y. Tan, R. Xie, S. Zhao, X. Lu, L. Liu, F. Zhao, C. Li, H. Jiang, G. Chai, D.J.L. Brett, P. R. Shearing, G. He, I.P. Parkin, Facile fabrication of robust hydrogen evolution electrodes under high current densities via Pt@Cu interactions, Adv. Funct. Mater. 31 (2021) 2105579, https://doi.org/10.1002/adfm.202105579.
[32] Y. Long, M. Wang, H. Zhao, W. Zhang, R. Dong, H. Wang, X. Wang, Self-assembled $NiMn_2O_4$ shell on nanoporous Ni(Mn) core for boosting alkaline hydrogen production, Appl. Surf. Sci. 614 (2023) 156152, https://doi.org/10.1016/j.apsusc.2022.156152.
[33] K. Dastafkan, X. Shen, R.K. Hocking, Q. Meyer, C. Zhao, Monometallic interphasic synergy via nano-hetero-interfacing for hydrogen evolution in alkaline electrolytes, Nat. Commun. 14 (2023) 547, https://doi.org/10.1038/s41467-023-36100-3.
[34] D.A. Porter, K.E. Easterling, M.Y. Sherif, Phase Transformations in Metals and Alloys, CRC Press, 2021.
[35] T.-J. Ko, K.H. Oh, M.-W. Moon, Plasma-induced hetero-nanostructures on a polymer with selective metal co-deposition, Adv. Mater. Interfaces 2 (2015) 1400431, https://doi.org/10.1002/admi.201400431.
[36] A.V. Tyunkov, E.M. Oks, Y.G. Yushkov, S.M. Zavadsky, D.B. Zolotukhin, Effects of gas pressure and bias potential on electron beam nitriding of titanium, J. Appl. Phys. 131 (2022) 213302, https://doi.org/10.1063/5.0089782.
[37] W. Liu, T. Xia, Y. Ye, H. Wang, Z. Fang, Z. Du, X. Hou, Self-supported Ni_3N nanoarray as an efficient nonnoble-metal catalyst for alkaline hydrogen evolution reaction, Int. J. Hydrog. Energy 46 (2021) 27037–27043, https://doi.org/10.1016/j.ijhydene.2021.05.188.
[38] G. Liu, F. Hou, Y. Wang, X. Wang, B. Fang, Engineering Ir and Ni_3N heterogeneous interfaces for promoted overall water splitting, Appl. Surf. Sci. 637 (2023) 157896, https://doi.org/10.1016/j.apsusc.2023.157896.
[39] Z. Qi, Y. Zeng, Z. Hou, W. Zhu, B. Wei, Y. Yang, B. Lin, H. Liang, Heterointerface engineering of Ni/Ni_3N hierarchical nanoarrays for efficient alkaline hydrogen evolution, Nano Res. 16 (2023) 4803–4811, https://doi.org/10.1007/s12274-022-5339-6.
[40] C. Li, F. Sun, X. Qin, K. Yang, W. Wu, A general strategy for Ni^0-NiOOH hybrid catalyst of high hydrogen evolution activity, Int. J. Hydrog. Energy 68 (2024) 491–498, https://doi.org/10.1016/j.ijhydene.2024.04.282.
[41] L. Xiong, Y. Qiu, H. Dong, B. Gao, X. Zhang, P.K. Chu, X. Peng, Metallic Ni_3N/Ni heterostructure for efficient hydrogen evolution reaction, Int. J. Hydrog. Energy 59 (2024) 400–407, https://doi.org/10.1016/j.ijhydene.2024.01.312.
[42] H.H. Do, M.A. Tekalgne, Q.V. Le, J.H. Cho, S.H. Ahn, S.Y. Kim, Hollow Ni/NiO/C composite derived from metal-organic frameworks as a high-efficiency electrocatalyst for the hydrogen evolution reaction, Nano Converg. 10 (2023) 6, https://doi.org/10.1186/s40580-023-00354-w.
[43] N. Attarzadeh, D. Das, S.N. Chintalapalle, S. Tan, V. Shutthanandan, C.V. Ramana, Nature-inspired design of nano-architecture-aligned Ni_5P_4-Ni_2P/NiS arrays for enhanced electrocatalytic activity of hydrogen evolution reaction (HER), ACS Appl. Mater. Interfaces 15 (18) (2023) 22036–22050, https://doi.org/10.1021/acsami.3c00781.
[44] Z. Qi, Y. Zeng, Z. Hou, W. Zhu, B. Wei, Y. Yang, B. Lin, H. Liang, Heterointerface engineering of Ni/Ni_3N hierarchical nanoarrays for efficient alkaline hydrogen evolution, Nano Res. 16 (2023) 4803–4811, https://doi.org/10.1007/s12274-022-5339-6.
[45] M. Liu, Z. Sun, C. Zhang, S. Li, C. He, Y. Liu, Z. Zhao, Multi-interfacial engineering of a coil-like NiS-Ni_2P/Ni hybrid to efficiently boost electrocatalytic hydrogen generation in alkaline and neutral electrolyte, J. Mater. Chem. A 297 (2021) 120455, https://doi.org/10.1016/j.apcatb.2021.120455.
[46] W. Li, K. Liu, S. Feng, Y. Xiao, L. Zhang, J. Mao, Q. Liu, X. Liu, J. Luo, L. Han, Well-defined Ni_3N nanoparticles armored in hollow carbon nanotube shell for high-efficiency bifunctional hydrogen electrocatalysis, J. Colloid Interface Sci. 655 (2024) 726–735, https://doi.org/10.1016/j.jcis.2023.11.069.
[47] G. Ma, P. Guo, S. Wang, Y. Liu, Y. Xin, H. Li, R. Chen, A. Wang, One-step plasma nitriding synthesis of Ni_xN/NF (x=3, 4) for efficient hydrogen evolution, Appl. Surf. Sci. 561 (2021) 149972, https://doi.org/10.1016/j.apsusc.2021.149972.
[48] F. Yuan, S. Wang, G. Yang, J. Qin, M. Chen, T. Fan, J. Ma, Construction of nickel sulfide phase-heterostructure for alkaline hydrogen evolution reaction, J. Colloid Interface Sci. 633 (2023) 640–648, https://doi.org/10.1016/j.jcis.2022.11.126.
[49] J.-T. Ren, Y.-S. Wang, Y.-J. Song, L. Chen, Z.-Y. Yuan, Interface engineering of in-situ formed nickel hydr(oxy)oxides on nickel nitrides to boost alkaline hydrogen electrocatalysis, Appl. Catal. B 309 (2022) 121279, https://doi.org/10.1016/j.apcatb.2022.121279.
[50] Y. Ni, X. Ma, S. Wang, Y. Wang, F. Song, M. Cao, C. Hu, Heterostructured nickel/vanadium nitrides composites for efficient electrocatalytic hydrogen evolution in neutral medium, J. Power Sources 521 (2022) 230934, https://doi.org/10.1016/j.jpowsour.2021.230934.
[51] X. Ding, D. Liu, P. Zhao, X. Chen, H. Wang, F.E. Oropeza, G. Gorni, M. Barawi, M. García-Tecedor, V.A. de la Peña O'Shea, J.P. Hofmann, J. Li, J. Kim, S. Cho, R. Wu, K.H.L. Zhang, Dynamic restructuring of nickel sulfides for electrocatalytic hydrogen evolution reaction, Nat. Commun. 15 (2024) 5336, https://doi.org/10.1038/s41467-024-49015-4.
[52] J. Li, Z. Zhu, Y. Huang, F. Wang, M.-S.(J.Tang) Balogun, Ni_3N: a multifunctional material for energy storage and electrocatalysis, Mater. Today Energy 26 (2022) 101001, https://doi.org/10.1016/j.mtener.2022.101001.
[53] J. Liu, D. Zhu, Y. Zheng, A. Vasileff, S.-Z. Qiao, Self-supported earth-abundant nanoarrays as efficient and robust electrocatalysts for energy-related reactions, ACS Catal. 8 (7) (2018) 6707–6732, https://doi.org/10.1021/acscatal.8b01715.
[54] J.M. Bockris, E. Potter, The mechanism of the cathodic hydrogen evolution reaction, J. Electrochem. Soc. 99 (4) (1952) 169–186, https://doi.org/10.1016/B978-1-4831-9831-6.50063-1.
[55] C.G. Morales-Guio, L.-A. Stern, X. Hu, Nanostructured hydrotreating catalysts for electrochemical hydrogen evolution, Chem. Soc. Rev. 43 (2014) 6555, https://doi.org/10.1039/C3CS60468C.
[56] L. Deng, L. Jin, L. Yang, C. Feng, A. Tao, X. Jia, Z. Geng, C. Zhang, X. Cui, J. Shi, Bubble evolution dynamics in alkaline water electrolysis, eScience 5 (4) (2025) 100353, https://doi.org/10.1016/j.esci.2024.100353.
[57] Y. Nie, T. Chen, M. Tian, Y. Zhang, X. Ruan, I.O. Baibars, D. Wei, C. Zhao, G. Zhang, A superaerophobic 3D array electrode promotes gas bubble management in alkaline water splitting, ACS Appl. Mater. Interfaces 17 (38) (2025) 53460–53469, https://doi.org/10.1021/acsami.5c12076.